Am J Nucl Med Mol Imaging 2022;12(1):1-14
www.ajnmmi.us /ISSN:2160-8407/ajnmmi0140939

Original Article

PET imaging of glycogen synthase kinase-3 in pancreatic cancer xenograft mouse models

Amanda J Boyle[1,2], Andrea Narvaez[1], Melissa Chassé[1,3], Neil Vasdev[1,2,3]

[1]Azrieli Centre for Neuro-Radiochemistry, Brain Health Imaging Centre, Centre for Addiction and Mental Health, Toronto, Ontario, M5T 1R8, Canada; [2]Department of Psychiatry, University of Toronto, Toronto, Ontario, M5T 1R8, Canada; [3]Institute of Medical Sciences, University of Toronto, Toronto, Ontario, M5S 1A8, Canada

Received December 3, 2021; Accepted January 9, 2022; Epub February 15, 2022; Published February 28, 2022

Abstract: Glycogen synthase kinase-3 (GSK-3) contributes to tumorigenesis in pancreatic cancer by modulating cell proliferation and survival. This study evaluated the lead GSK-3 targeted PET radiotracers for neuro-PET imaging, [^{11}C]PF-367 and [^{11}C]OCM-44, in pancreatic cancer xenograft mice. Immunohistochemistry showed that GSK-3α and GSK-3β were overexpressed in PANC-1 xenografts. In autoradiography studies, higher specific binding was observed for [^{3}H]PF-367 compared to [^{3}H]OCM-44 when co-incubated with unlabeled PF-367 (59.2±1.8% vs 22.6±3.75%, respectively). Co-incubation of [^{11}C]OCM-44 with OCM-44 did not improve the specific binding (25.5±30.2%). In dynamic PET imaging of PANC-1 xenograft mouse models, tumors were not visualized with [^{11}C]PF-367 but were well visualized with [^{11}C]OCM-44. Time-activity curves revealed no difference in accumulation in PANC-1 tumor tissue compared to muscle tissue in [^{11}C]PF-367 baseline studies, while a significant difference was observed for [^{11}C]OCM-44 with a tumor-to-muscle ratio of 1.6. Tumor radioactivity accumulation following injection with [^{11}C]OCM-44 was not displaced by pre-treatment with unlabeled PF-367. Radiometabolite analysis showed that intact [^{11}C]PF-367 accounted for 7.5% of tumor radioactivity, with >30% in plasma, at 40 min post-injection of the radiotracer, and that intact [^{11}C]OCM-44 accounted for 20% of tumor radioactivity, with >60% in plasma. [^{11}C]OCM-44 is superior to [^{11}C]PF-367 for detecting lesions in preclinical mouse models of pancreatic cancer, however, both radiotracers undergo rapid metabolism *in vivo*. GSK-3 PET radiotracers with improved in vivo stability are needed for clinical translation. To our knowledge this work represents the first PET imaging study of GSK-3 in oncology.

Keywords: Glycogen synthase kinase-3, pancreatic cancer, PET, carbon-11, GSK-3, oncology

Introduction

Pancreatic cancer (PnCa) is among the most lethal cancers and holds the highest mortality rate among all major cancers. It is the fourth leading cause of cancer-related deaths with a five-year survival rate of 10%, and a 75% mortality rate within the first year after diagnosis [1]. Few early symptoms are associated with pancreatic cancer, and the symptoms remain vague such as back pain, lethargy, and new onset diabetes [2]. In addition to being nearly asymptomatic, pancreatic cancer is very aggressive, such that patients are often at an advanced stage in disease progression at the time of initial diagnosis [3]. Less than 20% of pancreatic cancer patients are considered candidates for surgical resection due to tumor invasion of major blood vessels or metastases to the liver and/or other organs [4]. The high mortality rate of PnCa is largely due to a lack of biomarkers to diagnose the disease in its early stages when surgical removal of the tumor is still possible. New strategies for detection, diagnosis, and disease monitoring of PnCa are urgently needed.

Glycogen synthase kinase-3 (GSK-3) is a serine/threonine kinase that is responsible for the phosphorylation of many proteins [5]. GSK-3 is involved in multiple cell-signaling pathways with roles that can lead to pathogenesis of different diseases such as Alzheimer's disease and several cancers [6]. GSK-3 has many substrates and is therefore involved in numerous signal transduction pathways including NF-κB signaling [7], WNT/β-catenin signaling [8] and EGFR/RAS/PI3K/PTEN/AKT/GSK-3/mTORC1 pathway

[9]. The role of GSK-3 in cancer can be ambiguous such as both promoting and repressing cell proliferation, as well as acting as both a tumor suppressor and a tumor promoter, depending on the substrate. There are two isoforms of GSK-3, GSK-3α and GSK-3β, which have distinctive, non-redundant functions and both play a role in cancer cell survival, chemoresistance, and cancer progression in PnCa [9, 10]. Preclinical and clinical studies have investigated the use of GSK-3 inhibitors in PnCa as therapeutic agents, or as sensitizing agents to improve the efficacy of standard chemotherapies. In preclinical studies, the GSK-3 inhibitors AR-A014418 and SB-216763 were found to suppress PnCa growth *in vitro* and *in vivo* [11, 12] and the effect was increased when combined with gemcitabine [13, 14]; treatment with the GSK-3 inhibitor 9-ING-41 alone induced cell killing in PnCa cell lines and the cytotoxicity was significantly increased when combined with gemcitabine [15]. The GSK-3β inhibitor, tideglusib, was found to suppress proliferation of PnCa cells [16]. *In vivo* studies showed that treatment with the GSK-3α/β inhibitor LY2090314 in combination with the chemotherapy Nab-pablitaxal (Abraxane®) improved survival in mice bearing AsPC-1 PnCa orthotopic xenografts [17]. A clinical trial was initiated to administer LY2090314 in patients with metastatic cancer, including advanced PnCa (ClinicalTrials.gov identifier: NCT01632306) and a trial using 9-ING-41 for advanced cancers including PnCa is underway (ClinicalTrials.gov identifier: NCT03678883). A positron emission tomography (PET) radiotracer capable of quantifying GSK-3 density and distribution *in vivo* could provide new strategies for detection, diagnosis, and disease monitoring of PnCa.

Our laboratories reported the first radiotracer for imaging GSK-3, [^{11}C]AR-A014418 [18]. Several PET radiotracers targeting GSK-3 have been subsequently reported (**Figure 1**) and evaluated in preclinical brain-PET imaging studies [19-26]. The most promising radiotracers for imaging GSK-3α/β are oxazole-4-carboxamides, [^{11}C]PF-04802367 ([^{11}C]PF-367) and its derivative [^{11}C]OCM-44, that we developed with high affinity and selectivity for GSK-3α/β [27-29]. Despite extensive efforts to image GSK-3 in the brain, to date a PET radiotracer targeting GSK-3 has not yet been explored to visualize cancer tumors *in vivo*. This study evaluates [^{11}C]PF-367 and [^{11}C]OCM-44 in PnCa xenograft mouse models by immunohistochemistry (IHC), autoradiography, dynamic PET/MR imaging including blocking studies, *ex vivo* biodistribution, and radiometabolite analysis.

Materials and methods

General

Tritium labeled PF-04802367 ([^{3}H]PF-367; molar activity (A_m) =3000 GBq/mmol (81 Ci/mmol), 37 MBq/mL (1 mCi/mL), radiochemical purity (RCP) =87.5%) and 5-(3-fluoro-4-methoxyphenyl)-N-(3-(pyridin-3-yl)propyl)oxazole-4-carboxamide ([^{3}H]OCM-44; A_m=3000 GBq/mmol (81 Ci/mmol), 37 MBq/mL (1 mCi/mL), RCP=87.4%) were prepared by tritiomethylation from the respective desmethyl precursors at Novandi Chemistry AB (Södertälje, Sweden). PF-04802367 was purchased commercially (Millipore Sigma). Radiolabeling precursors and unlabeled OCM-44 were prepared by Sai Life Sciences, Ltd (Hyderabad, India).

Radiochemical synthesis of [^{11}C]PF-367 and [^{11}C]OCM-44

Automated radiosynthesis of [^{11}C]PF-367 was carried out on a GE Tracerlab FX2 C-Pro™ synthesis module as previously described [28] with modifications to adapt a "loop method" [30]. Briefly, the HPLC loop was pre-loaded with desmethyl-PF-367 (0.5±0.1 mg) dissolved in 100 μL anhydrous MEK and 2.5 μL 1.0 M methanolic TBAOH. [^{11}C]CH_3OTf was flowed through the HPLC loop for 3 min at room temperature (RT) prior to injection onto a semi-preparative Luna® C18(2) HPLC column (10 μm, 10×250 mm; Phenomenex, Torrance, USA). Isocratic semi-preparative HPLC purification was conducted at 5.0 mL/min with 40/60 CH_3CN/100 mM NH_4HCO_2 (v/v) as the mobile phase. The peak corresponding to [^{11}C]PF-367 was collected and diluted with a sterile mixture of 20 mL H_2O and 2 mL 1 M $NaHCO_3$. The diluted solution was passed through a pre-conditioned solid-phase extraction cartridge (SepPak® tC18 Plus, Waters; Milford, USA) and the cartridge was rinsed with 10 mL of sterile water. The radiotracer was eluted with 1 mL EtOH, followed by 9 mL 0.9% saline. Analytical HPLC was performed at 1.0 mL/min with 40/60 CH_3CN/100 mM NH_4HCO_2 (v/v) mobile phase on a Luna

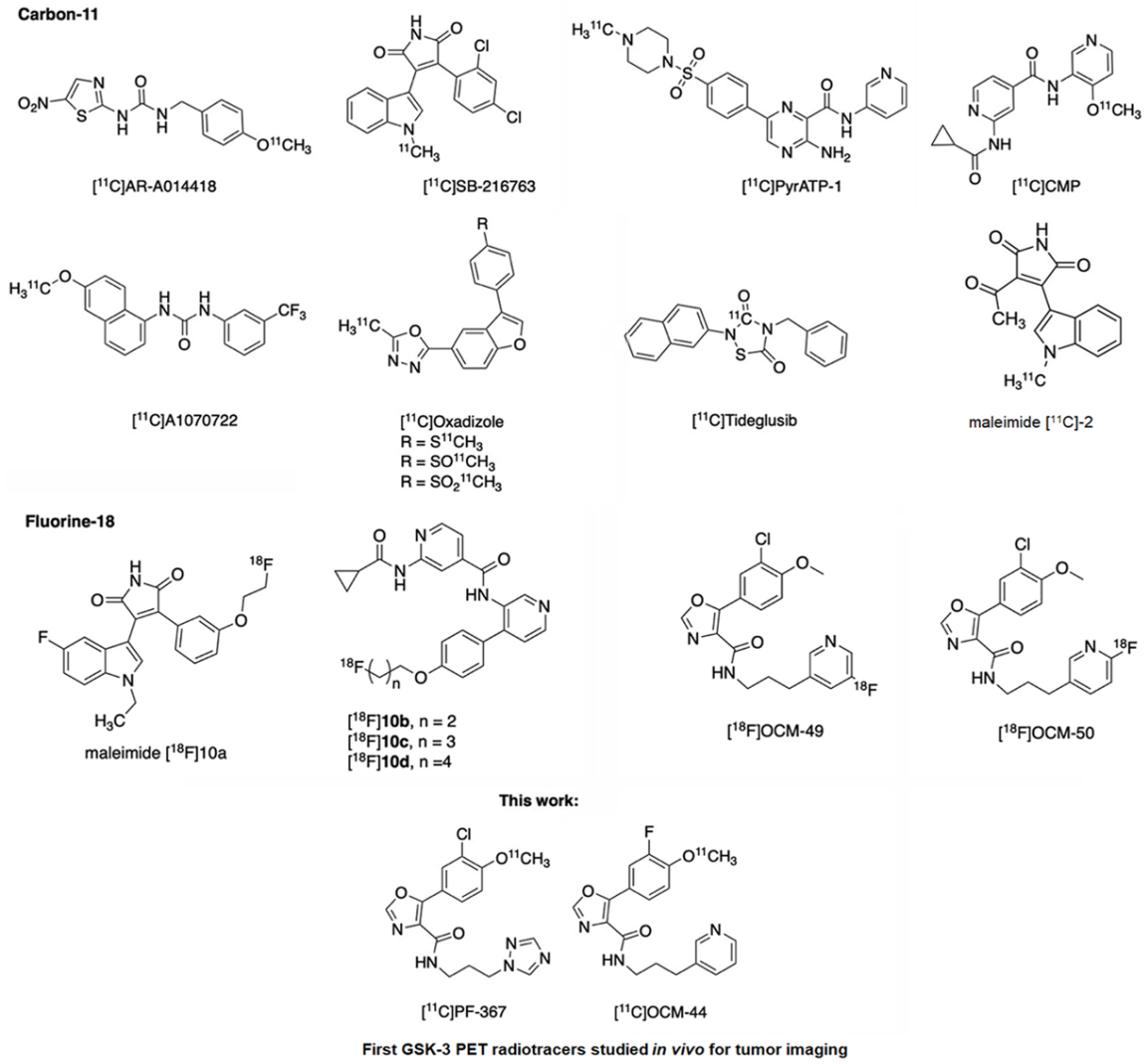

Figure 1. PET radiotracers for imaging GSK-3. See [25, 26] and references cited therein.

C18 HPLC column (10 μm, 4.6×250 mm; Phenomenex).

Automated radiosynthesis of [^{11}C]OCM-44 was also carried out on a GE Tracerlab FX2 C-Pro™ synthesis module as previously described [28] with minor modifications to adapt a "loop method" [30]. Briefly, 1.0±0.1 mg of desmethyl-OCM-44 was dissolved in 80 μL anhydrous DMF, then 1.5 μL potassium *tert*-butoxide (1 M in THF) was added. This solution was pre-loaded on a 5 mL stainless-steel loop, 5 min prior to radiosynthesis. [^{11}C]CH_3I was flowed through the stainless-steel loop and held at RT for 5 min prior to being loaded onto a semi-preparative Luna C18 HPLC column (10 μm, 10×250 mm; Phenomenex) for isocratic separation with 40/60 CH_3CN/H_2O + 0.1 N ammonium formate as the mobile phase. The peak corresponding to [^{11}C]OCM-44 was collected and diluted with a sterile mixture of 20 mL H_2O and 2 mL 1 M $NaHCO_3$. The diluted solution was passed through a pre-conditioned solid-phase extraction cartridge (SepPak® tC18 Plus, Waters) and the cartridge was rinsed with 10 mL of sterile water. The radiotracer was eluted with 1 mL EtOH, followed by 9 mL 0.9% saline. Analytical HPLC was performed at 3.0 mL/min with 40/60 CH_3CN/100 mM NH_4HCO_2 (v/v) mobile phase on a Luna C18 HPLC column (10 μm, 4.6×250 mm; Phenomenex).

Tumor xenograft mouse models

PANC-1 human PnCa cells, with high GSK-3α and GSK-3β expression [12, 31], were purchased from the American Type Culture Collection (Manassas, VA, USA). PANC-1 cells were

cultured in McCoy's 5A Modified medium (Gibco, Life Technologies; Burlington, ON, Canada) supplemented with 10% fetal bovine serum (Gibco), and 1% penicillin/streptomycin (Sigma-Aldrich, St. Louis, MO, USA). Cells were cultured in an atmosphere of 5% CO_2 at 37°C. Female ICRscid mice (Taconic Biosciences; Rensselaer, NY, USA), were inoculated subcutaneously (s.c.) on the right flank and imaged when tumors reached 0.75-1.0 cm diameter. Animal studies were conducted under a protocol (#817) approved by the Animal Care Committee at the Centre for Addition and Mental Health, following Canadian Council on Animal Care guidelines.

Immunohistochemistry

IHC was performed to determine GSK-3α and GSK-3β density in PANC-1 tumors. Tumors were fixed in 10% formalin for 48 h then embedded in paraffin and prepared in 4 μm sections onto microscope slides. Slides were dewaxed through changes of xylene, followed by hydration through decreasing grades of alcohol in water (100%, 95%, 70%). Slides were blocked with 3% hydrogen peroxide then antigen retrieval was performed with pepsin for slides being stained for CD68. Serum block was applied as per directed by the MACH-4 Universal HRP-Polymer kit (Inter Medico, Markham, ON, CA) followed by incubation with primary antibodies mouse anti-CD68 (M0876, 1:400; Agilent Dako, Santa Clara, CA, USA), rabbit polyclonal anti-GSK-3α (Ab62331, 1:200; Abcam, Cambridge, UK), or rabbit recombinant anti-GSK-3β (phosphor S9) antibody (Ab75814, 1:100; Abcam) at RT for 1 h. Color was developed using DAB (K3468, Agilent Dako) and counter stained with hematoxylin. Slides were dehydrated by reversing the rehydration procedure and sections were mounted with mounting medium (3801120, Leica, Buffalo Grove, IL, USA). Slides were scanned with a slide scanner (VS200 Slideview, Olympus, Tokyo, Japan).

Autoradiography

Tumors were excised and immediately stored at -80°C until cryostat sectioning. Frozen tumors were coated with Tissue-Tek (Sakura Finetek, Tokyo, Japan) embedding medium for frozen tissue specimens to ensure the optimal cutting temperature (O.C.T.), a serial of 10 μm thick cryosections was generated using a Cryostar NX50 cryostat (Thermo Fisher Scientific, Runcorn, UK). Slides were stored at -80°C until receptor binding assays were performed. Prior to autoradiography studies, tissue sections were removed from freezing conditions and acclimated to RT for 30 min.

For total binding, slides were incubated for 60 min at RT with 8 nM [^{3}H]PF-367 or [^{3}H]OCM-44 in HEPES-buffered Krebs-Ringer Solution, pH 7.2 containing DMSO (Invitrogen, Oregon, USA). For non-specific binding, slides were incubated for 60 min at RT with 8 nM [^{3}H]PF-367 or [^{3}H]OCM-44 in HEPES-buffered Krebs-Ringer Solution, pH 7.2, adding 10 μM unlabeled DMSO-dissolved PF-367 or OCM-44. Slides were washed with ice-cold 0.9% saline once for 60 seconds followed by a 10-second rinse with ice-cold distilled water. Slides were dried under airflow.

After incubating with the tritium labeled radiotracers, washing, and drying, the tissue sections and tritium standard (ART 0123A, American Radiolabeled Chemicals, Missouri, USA) were placed into a Halsey Rigidform Cassette (Halsey X-Ray Products, New York, USA) and exposed to a TR2040 phosphor screen (FUJIFILM, Tokyo, Japan) for five days at RT, then scanned using an Amersham Typhoon™ Biomolecular Imager (GE Healthcare, Massachusetts, USA). Receptor binding was quantified (nCi/mg) using a Microcomputer Imaging Device (MCID) computer-based imaging system 7.1 (Imaging Research Inc., Ontario, CA) based on the tritium standard exposed with the slides. Non-specific binding was subtracted from total binding to calculate specific binding.

Dynamic PET/MR imaging and biodistribution studies

PET/magnetic resonance (MR) image acquisition and analysis were performed as previously described [32]. Tumor-bearing mice were anesthetized by isoflurane in O_2 (4%, 2 L/min induction; 1-2%, 1 L/min maintenance) for lateral tail-vein catheterization then transferred to a nanoScan™ PET/MRI 3T scanner (Mediso, Budapest, Hungary). Anesthesia was maintained throughout PET/MR scanning while body temperature and respiration parameters were monitored. Mice bearing PANC-1 xenografts were injected through the tail-vein catheter with [^{11}C]PF-367 (2.1-9.18 MBq, 5.47-44.15 nmol/kg,

3.72-24.93 GBq/μmol) or [^{11}C]OCM-44 (6.17-12.77 MBq, 0.53-22.45 nmol/kg, 63.36-368.94 GBq/μmol). For blocking studies, mice bearing PANC-1 xenografts were scanned at baseline (*n*=2 for [^{11}C]PF-367; *n*=5 for [^{11}C]OCM-44) or under blocking conditions (*n*=2), in which mice were pre-treated with an i.p. injection of 2 mg unlabeled PF-367 in 20 μL dimethylsulfoxide (Sigma) 60 min prior to bolus injection of [^{11}C]PF-367 or [^{11}C]OCM-44. Following the 60 min PET scans, mice were sacrificed by cervical dislocation and tissue samples were collected, weighed, and transferred to γ-counting tubes for biodistribution analysis. Tissue radioactivity was measured with a γ-counter (2480 Wizard^{2}™, PerkinElmer, MA, USA) and expressed as % ID/g. Image analyses and extraction of time-activity curves (TACs) from regions of interest (ROIs) were performed in Amide v1.0.4.

Radiometabolite analysis

Tumor-bearing mice were sacrificed by cervical dislocation 40 min post-injection (p.i.) with [^{11}C]PF-367 (*n*=1, 10.4 MBq, 2.82 nmol/kg, 97.13 GBq/μmol) or [^{11}C]OCM-44 (*n*=1, 4.85 MBq, 412.46 nmol/kg, 0.32 GBq/μmol). Blood was collected by cardiac heart puncture then centrifuged for 5 min at 2,000× RCF. Tumors were excised and homogenized with a BeadBug™ (Benchmark Scientific; Sayreville, NJ, USA) in 1.6 mL acetonitrile with respective 50 ng of unlabeled parent compounds PF-367 or OCM-44, then 0.8 mL H_2O was added. The homogenate was centrifuged at 10,000× RCF for 5 min. Parent radiotracer was separated from plasma and tumor homogenates by column-switching HPLC in a mobile phase of 40/60 CH_3CN/100 mM NH_4HCO_2 (v/v), as previously described by our laboratories [32], and analyzed with PowerChrom 2.6.15 (eDAQ) [33].

Statistical analysis

Data are represented as the mean ± SD. Statistical comparisons were performed by an unpaired t-test (P<0.05) with GraphPad Prism Version 9.

Results

Radiosynthesis of [^{11}C]PF-367 and [^{11}C]OCM-44

[^{11}C]PF-367 was produced and had a retention time of approximately 9.5-10.5 min during the semi-preparative purification (**Figure 2A** and **2B**). [^{11}C]PF-367 was synthesized with RCP> 99%, as confirmed by co-elution of the formulated radiotracer with authentic PF-367 standard by analytical HPLC (**Figure 2C** and **2D**). [^{11}C]PF-367 had an average A_m=41.4 GBq/μmol (*n*=5, 1119 mCi/μmol).

[^{11}C]OCM-44 was separated by semi-preparative HPLC with a retention time of approximately 11.7-12.7 min (**Figure 3A** and **3B**). [^{11}C]OCM-44 was synthesized with a average A_m=161.3 GBq/μmol (*n*=8, 4360 mCi/μmol) and RCP> 99%, as confirmed by co-elution of authentic standard by analytical HPLC (**Figure 3C** and **3D**).

Immunohistochemistry

GSK-3α and GSK-3β density were examined by IHC staining in human PnCa PANC-1 xenografts (**Figure 4**). IHC staining confirmed that PANC-1 xenografts had high expression (brown staining) of GSK-3α and GSK-3β. Tissue sections of PANC-1 tumors were also analyzed for CD-68, a surface biomarker on cells of human macrophage/monocyte origin, as a negative control.

Autoradiography

Figure 5 depicts the results of autoradiography studies which assessed the specific binding of [^{3}H]PF-367 and [^{3}H]OCM-44 co-incubated with unlabeled PF-367 or OCM-44 in PANC-1 tumor tissue sections. Co-incubation of 8 nM [^{3}H]PF-367 with 10 μM unlabeled PF-367 on PANC-1 tumor sections exhibited specific binding of 59.2±1.8%, which was reduced, though not significantly, to 48.9±12.0% when co-incubated with 10 μM unlabeled OCM-44. No difference in specific binding was observed when [^{3}H]OCM-44 was co-incubated with 10 μM unlabeled PF-367 or OCM-44, 22.6±3.75% and 25.5±30.2%, respectively. The specific binding of [^{3}H]PF-367 was significantly higher than [^{3}H]OCM-44 in PANC-1 tumor tissues when co-incubated with PF-367 (P=0.0001). No significant difference was observed between [^{3}H]PF-367 or [^{3}H]OCM-44 in PANC-1 tumor tissues when co-incubated with OCM-44.

Dynamic PET/MR imaging of tumor-bearing mice

We evaluated [^{11}C]PF-367 and [^{11}C]OCM-44 in ICRscid mice bearing s.c. PANC-1 PnCa xeno-

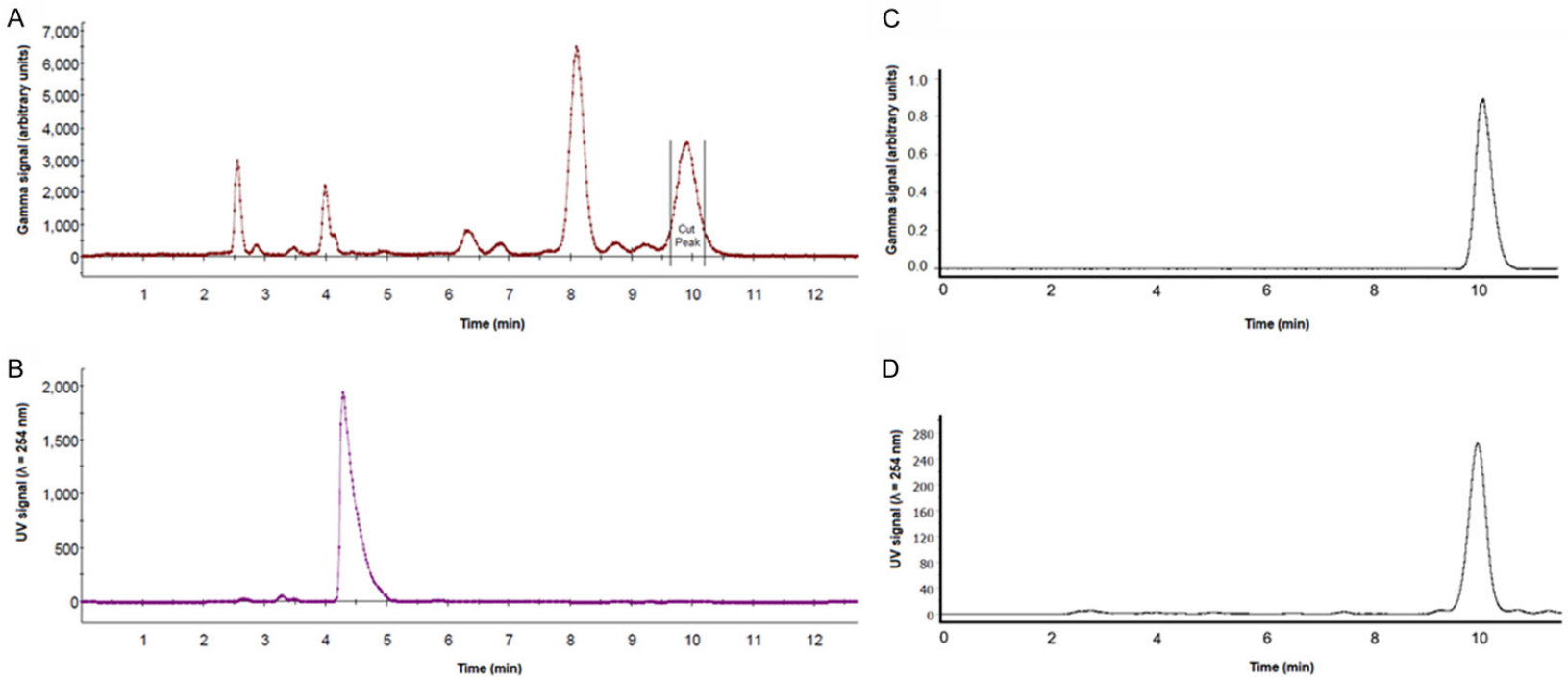

Figure 2. HPLC chromatograms from the production of [^{11}C]PF-367. Semi-preparative HPLC chromatogram of (A) radioactive (gamma) signal and (B) UV signal. Analytical HPLC chromatograms showing (C) radioactive (gamma) signal from the formulated radiotracer and (D) UV signal from the authentic PF-367 reference standard.

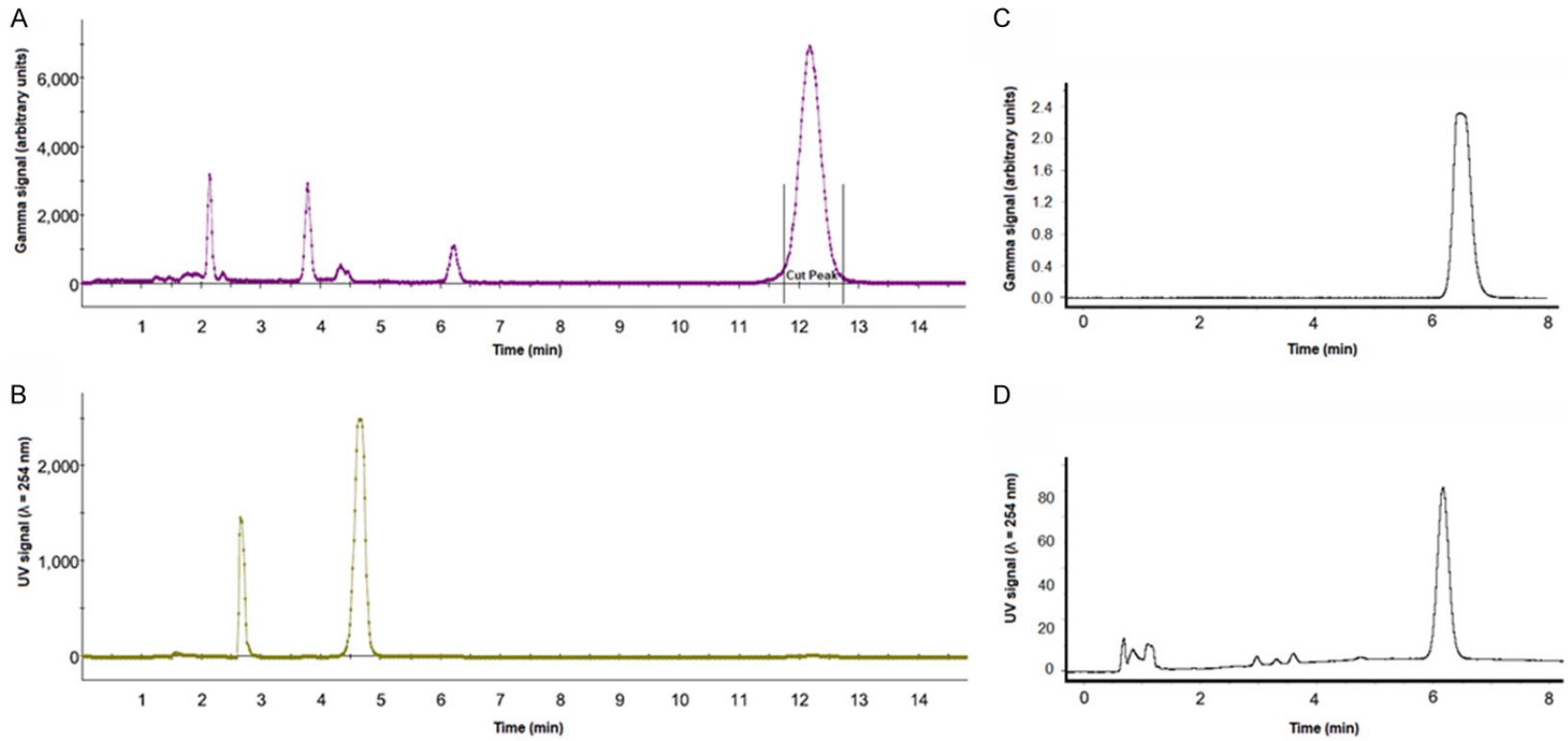

Figure 3. HPLC chromatograms from the production of [^{11}C]OCM-44. Semi-preparative HPLC chromatogram of (A) radioactive (gamma) signal and (B) UV signal. Analytical HPLC chromatograms showing (C) radioactive (gamma) signal from the formulated radiotracer and (D) UV signal from the authentic OCM-44 reference standard.

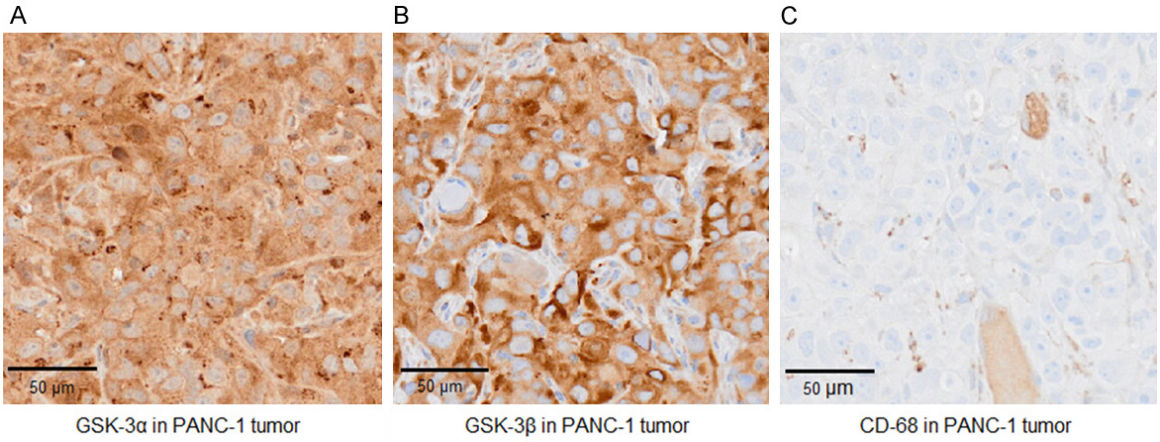

Figure 4. GSK-3α, GSK-3β, and CD-68 expression in PANC-1 PnCa xenograft tissue sections. IHC staining shows high expression of (A) GSK-3α and (B) GSK-3β, and (C) low expression of CD-68 in PANC-1 PnCa xenografts.

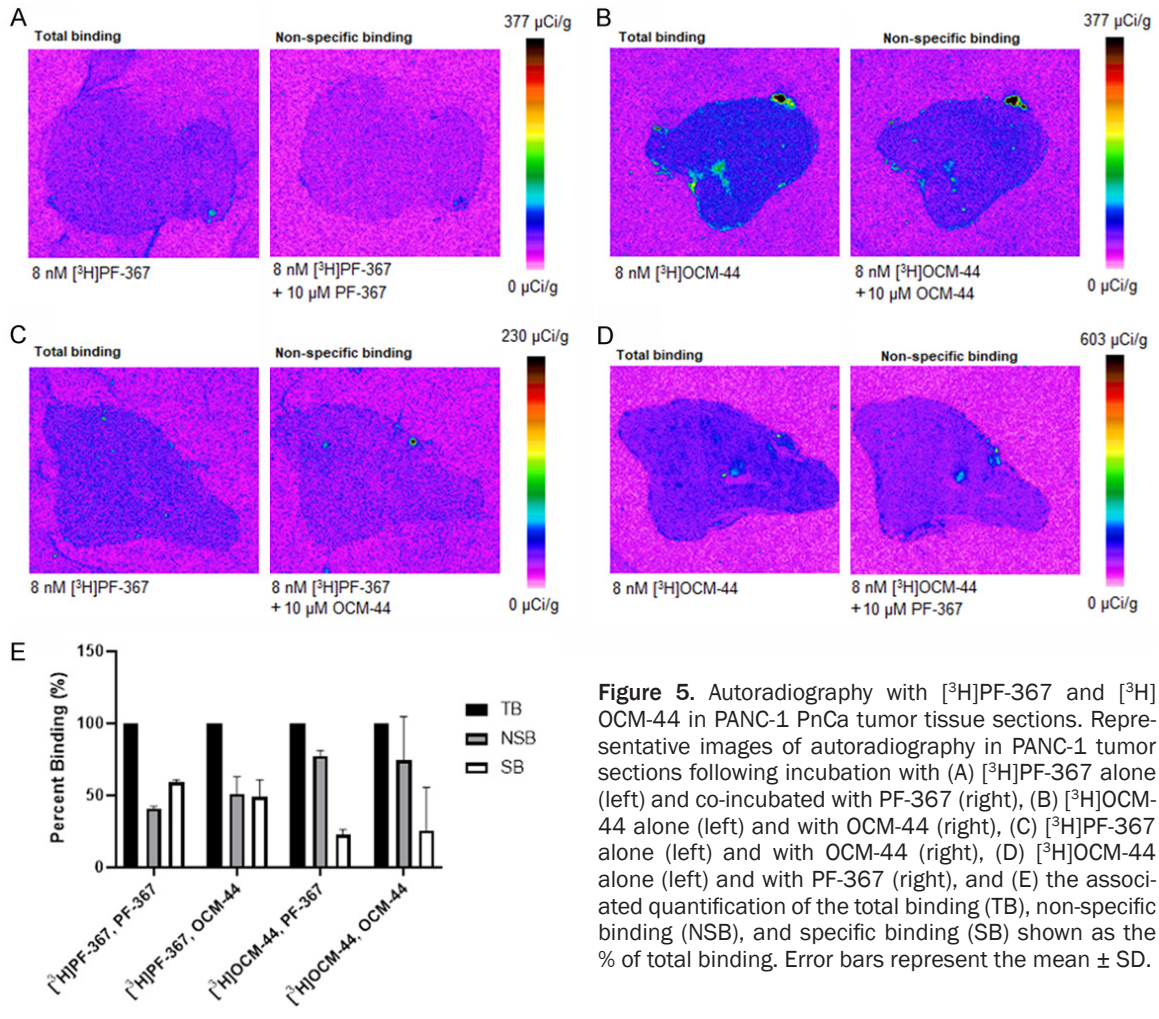

Figure 5. Autoradiography with [^{3}H]PF-367 and [^{3}H]OCM-44 in PANC-1 PnCa tumor tissue sections. Representative images of autoradiography in PANC-1 tumor sections following incubation with (A) [^{3}H]PF-367 alone (left) and co-incubated with PF-367 (right), (B) [^{3}H]OCM-44 alone (left) and with OCM-44 (right), (C) [^{3}H]PF-367 alone (left) and with OCM-44 (right), (D) [^{3}H]OCM-44 alone (left) and with PF-367 (right), and (E) the associated quantification of the total binding (TB), non-specific binding (NSB), and specific binding (SB) shown as the % of total binding. Error bars represent the mean ± SD.

grafts by dynamic PET/MR imaging and validated the PET scan data analysis by *ex vivo* biodistribution studies. **Figure 6A** shows a representative PET image of a mouse bearing a s.c. PANC-1 xenograft following injection with [^{11}C]PF-367 (0-60 min summed image) and did

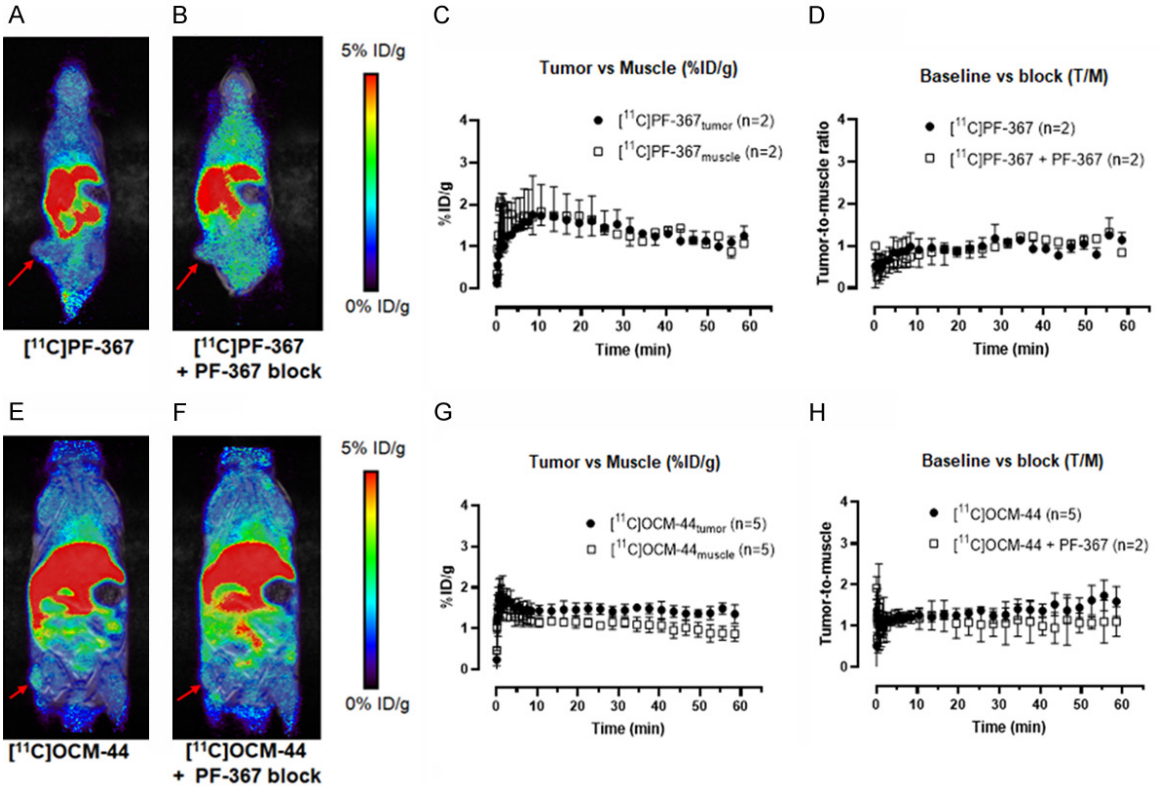

Figure 6. Dynamic PET/MR imaging and TACs of GSK-3 targeted [^{11}C]PF-367 and [^{11}C]OCM-44 in PANC-1 PnCa xenograft mouse models. Representative iterative static PET/MR images (0-60 min summed image) of [^{11}C]PF-367 at (A) baseline, (B) with PF-367 blockade, and (C, D) respective TACs. Representative iterative static PET/MR images (0-60 min summed image) of [^{11}C]OCM-44 at (E) baseline, (F) with PF-367 blockade, and (G, H) respective TACs. Tumor sites are indicated by red arrows.

not reveal radioactivity accumulation in the tumor. Analysis of TACs support that the image acquired at baseline showed no difference between radioactivity accumulation in the tumor and in muscle tissue (**Figure 6C**). Blocking studies were performed by pre-treatment with unlabeled PF-367 prior to [^{11}C]PF-367 bolus injection and revealed no difference between the tumor/muscle (T/M) ratios under baseline and blocked conditions (**Figure 6D**). **Figure 6E** shows a representative PET image of a mouse bearing a s.c. PANC-1 xenograft following injection with [^{11}C]OCM-44 (0-60 min summed image) in which the tumor was well visualized. However, as shown in **Figure 6F**, the radioactivity accumulation in the tumor was not displaced by pre-treatment with unlabeled PF-367. **Figure 6G** shows that the TAC analysis of [^{11}C]OCM-44 at baseline confirms a significantly higher tumor tissue radioactivity accumulation compared to muscle tissue with an average uptake from 50-60 min of 1.41±0.16% ID/g vs 0.91±0.19% ID/g (P=0.0022) resulting in 1.6 T/M. **Figure 6H** shows the TAC analysis of blocking studies performed by pre-treatment with unlabeled PF-367 prior to bolus [^{11}C]OCM-44 injection and reveals a decrease between the T/M at baseline or blocked conditions, 1.60±0.30% ID/g vs 1.09±0.31% ID/g, albeit the result is not statistically different (P= 0.1040).

PET imaging analyses were substantiated by *ex vivo* biodistribution studies of selected tissues performed 60 min following radiotracer injection. No difference between radioactivity accumulation in tumor tissue and muscle tissue was observed for [^{11}C]PF-367 (1.39±0.17% ID/g and 1.31±0.36% ID/g, respectively, (P= 0.785)). Radioactivity accumulation in tumor tissue was significantly higher than that in muscle tissue for [^{11}C]OCM-44 (1.11±0.08% ID/g and 0.59±0.09% ID/g, (P=0.0236)). The resultant tumor-to-muscle ratios for [^{11}C]PF-367 and [^{11}C]OCM-44 were 1.1 and 1.9, respectively. No significant difference was obser-

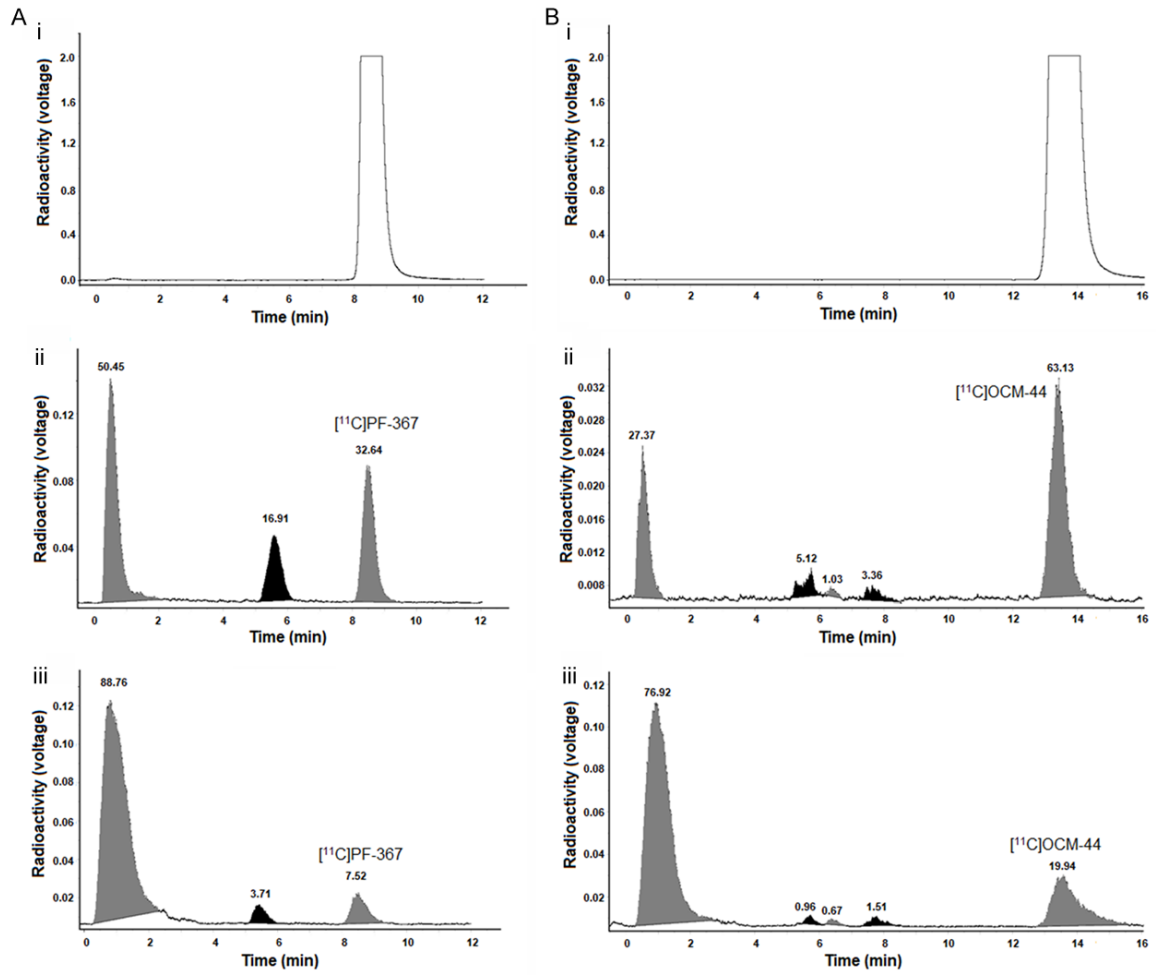

Figure 7. Radiometabolite analysis of [^{11}C]PF-367 and [^{11}C]OCM-44 in PANC-1 tumor-bearing mice at 40 min p.i. (A) Column-switching HPLC chromatogram of [^{11}C]PF-367 (i) product following radiosynthesis; HPLC chromatogram with normalized peak analysis from (ii) plasma and (iii) tumor homogenates. (B) Column-switching HPLC chromatogram of [^{11}C]OCM-44 (i) product following radiosynthesis; HPLC chromatogram with normalized peak analysis from (ii) plasma and (iii) tumor homogenates.

ved in tumor radioactivity accumulation of [^{11}C]PF-367 or [^{11}C]OCM-44, which revealed 1.39±0.17% ID/g and 1.11±0.08% ID/g, respectively (P=0.1634). Additionally, tumor radioactivity accumulation of [^{11}C]PF-367 and [^{11}C]OCM-44 when pre-treated with unlabeled PF-367 blockade were observed at 1.39±0.72% ID/g and 1.30±0.40% ID/g, respectively, and were not significantly different from their respective baselines (P=0.9924 and P=0.5865).

Radiometabolite analysis

Ex vivo composition of [^{11}C]PF-367 and [^{11}C]OCM-44 in plasma and tumor tissue were determined at 40 min p.i. in tumor-bearing mice by HPLC analysis of relative amounts of parent radioligand and radiometabolites. At 40 min p.i., intact [^{11}C]PF-367 (**Figure 7A**) represented 32.6% of the total radioactivity in the plasma and 7.5% in tumor tissue while intact [^{11}C]OCM-44 (**Figure 7B**) represented 63.1% of the total radioactivity in the plasma and 19.9% in tumor tissue. These results indicate that [^{11}C]PF-367 is metabolized at a faster rate than [^{11}C]OCM-44 yet both radiotracers exhibit rapid metabolism in mice.

Discussion

Radiotracers with high selectivity and affinity for GSK-3 have been sought after and optimized for brain-PET imaging for nearly two decades [18]. The two lead GSK-3 PET radio-

tracers to date are [^{11}C]PF-367 and [^{11}C]OCM-44, which have high selectivity and affinity for GSK-3. In light of the increased applications of these PET radiotracers we simplified the automated radiosynthesis on a commercial platform, by adapting the "loop method" for ^{11}C-methylation reactions with and [^{11}C]CH_3OTf and [^{11}C]CH_3I, for [^{11}C]PF-367 and [^{11}C]OCM-44, respectively. Preliminary evaluation of [^{11}C]CH_3OTf, compared with [^{11}C]CH_3I, for alkylation of [^{11}C]PF-367 suppressed the formation of a volatile impurity and led to higher RCYs (not optimized). In the present study, we sought to evaluate [^{11}C]PF-367 and [^{11}C]OCM-44 as the first PET radiotracers targeting GSK-3 in oncology. We thereby directed our efforts to visualize PnCa tumors in xenograft mouse models.

In agreement with the literature, our IHC studies showed that both GSK-3α and GSK-3β are present and evenly distributed through PANC-1 PnCa xenografts [12]. In autoradiography studies using PANC-1 PnCa xenograft tissue, higher specific binding of [^{3}H]PF-367 for GSK-3 was observed compared to [^{3}H]OCM-44, with 2.6-fold greater specific binding when blocked with PF-367 and 2-fold greater specific binding when blocked with OCM-44. Despite high selectivity and specific binding observed *ex vivo* in PANC-1 xenografts incubated with [^{3}H]PF-367, no radioactivity accumulation was observed in PANC-1 tumors *in vivo* by PET imaging with [^{11}C]PF-367. The lack of tumor uptake following administration of [^{11}C]PF-367 in PET imaging studies is rationalized by its extensive radiometabolism in mice despite reports of reasonable *in vitro* stability in human hepatic microsomes [27], with only 7.5% of the radioactivity accumulated in the tumor accounted for by intact parent [^{11}C]PF-367 after 40 min. PET imaging studies with [^{11}C]OCM-44 revealed a T/M of 1.6. However, the tumor uptake could not be displaced in blocking studies with pre-treatment of PF-367, which may be attributed to the rapid metabolism of both PF-367 and OCM-44 in mice. Radiometabolite analysis from arterial blood for both of these tracers is underway in non-human primates and will be published elsewhere with detailed kinetic analysis.

A limitation of this study is the lack of potent and selective GSK-3 inhibitors with reasonable metabolic stability available for blocking studies. Although excess unlabeled PF-367 was used to block the radioactivity accumulation of [^{11}C]PF-367 and [^{11}C]OCM-44, the use of unlabeled OCM-44 or other newer generation GSK-3 inhibitors with slower metabolism are likely needed to adequately confirm specificity of radiotracer binding. The rapid metabolism observed with [^{11}C]PF-367 and [^{11}C]OCM-44 may restrict their applications in PET imaging of oncology. A lack of suitable inhibitors for demonstrating *in vivo* selectivity of novel targets can present an obstacle to discovering and screening lead radiotracers for PET imaging novel biomarkers [34]. Furthermore, the roles of GSK-3α and GSK-3β in PnCa are not functionally redundant despite their structural similarity. In NF-κB cell signaling, GSK-3α inhibition leads to suppression of cell growth in PnCa [35], while GSK-3β up-regulates NF-κB activity which stimulates cell proliferation, protumorigenic cytokine production, resistance to apoptosis, and chemoresistance in PnCa [12, 36-38]. GSK-3β is also involved in the WNT/β-catenin pathway by modulating resistance to radiation therapy [39]. Future studies investigating GSK-3 in PnCa with a PET radiotracer that is selective for GSK-3α or -β would also be worthwhile to investigate in oncology as newer generations of GSK-3 PET radiotracers are discovered [28].

Conclusions

To our knowledge this works represents the first PET imaging study of GSK-3 in cancer. Herein we simplified the automated radiosynthesis of the two leading GSK-3 PET radiotracers, [^{11}C]PF-367 and [^{11}C]OCM-44 to adapt the "loop method" for ^{11}C-methylation. [^{11}C]OCM-44 was utilized to successfully image GSK-3 overexpressing PnCa tumors in PANC-1 xenograft mouse models. Although the rapid metabolism in the periphery and short half-life of the radionuclide may preclude the use of [^{11}C]PF-367 and [^{11}C]OCM-44 in oncology, next generation GSK-3 and related kinase inhibitors have potential for imaging signal transduction pathways.

Acknowledgements

We thank our colleagues at the CAMH Brain Health Imaging Centre for support with the cyclotron, radiochemistry, and preclinical research. AJB acknowledges support from the

CAMH Discovery Fund. AN is supported by Enigma Biomedical Group. MC is a recipient of an Ontario Graduate Scholarship and a Canadian Institute of Health Research Master's Program Scholarship. NV thanks the National Institute on Ageing of the NIH (R01AG054473), the Azrieli Foundation, the Canada Research Chairs Program, Canada Foundation for Innovation, and the Ontario Research Fund for support.

Disclosure of conflict of interest

NV is a co-founder of MedChem Imaging, Inc. and serves as an Advisory Board Member for 4M Therapeutics, Inc. The above-mentioned interests had no role in the design and conduct of the study; collection, management, analysis, and interpretation of the data; preparation, review, or approval of the manuscript; and decision to submit the manuscript for publication. All other authors declare no potential conflict of interest.

Address correspondence to: Amanda J Boyle and Neil Vasdev, Azrieli Centre for Neuro-Radiochemistry, Brain Health Imaging Centre, Centre for Addiction and Mental Health, Toronto, Ontario, M5T 1R8, Canada. Tel: 416-535-8501 Ext. 30884; E-mail: amy.boyle@camh.ca (AJB); neil.vasdev@utoronto.ca (NV)

References

[1] Siegel RL, Miller KD, Fuchs HE and Jemal A. Cancer statistics, 2021. CA Cancer J Clin 2021; 71: 7-33.

[2] Keane MG, Horsfall L, Rait G and Pereira SP. A case-control study comparing the incidence of early symptoms in pancreatic and biliary tract cancer. BMJ Open 2014; 4: e005720.

[3] Vincent A, Herman J, Schulick R, Hruban RH and Goggins M. Pancreatic cancer. Lancet 2011; 378: 607-20.

[4] Gillen S, Schuster T, Meyer Zum Buschenfelde C, Friess H and Kleeff J. Preoperative/neoadjuvant therapy in pancreatic cancer: a systematic review and meta-analysis of response and resection percentages. PLoS Med 2010; 7: e1000267.

[5] Kockeritz L, Doble B, Patel S and Woodgett JR. Glycogen synthase kinase-3--an overview of an over-achieving protein kinase. Curr Drug Targets 2006; 7: 1377-88.

[6] McCubrey JA, Steelman LS, Bertrand FE, Davis NM, Sokolosky M, Abrams SL, Montalto G, D'Assoro AB, Libra M, Nicoletti F, Maestro R, Basecke J, Rakus D, Gizak A, Demidenko Z, Cocco L, Martelli A and Cervello M. GSK-3 as potential target for therapeutic intervention in cancer. Oncotarget 2014; 5: 2881-911.

[7] Bang D, Wilson W, Ryan M, Yeh JJ and Baldwin AS. GSK-3α promotes oncogenic KRAS function in pancreatic cancer via TAK1-TAB stabilization and regulation of noncanonical NF-κB. Cancer Discov 2013; 3: 690-703.

[8] Ram Makena M, Gatla H, Verlekar D, Sukhavasi S, Pandey MK and Pramanik KC. Wnt/β-catenin signaling: the culprit in pancreatic carcinogenesis and therapeutic resistance. Int J Mol Sci 2019; 20: 4242.

[9] Duda P, Akula SM, Abrams SL, Steelman LS, Martelli AM, Cocco L, Ratti S, Candido S, Libra M, Montalto G, Cervello M, Gizak A, Rakus D and McCubrey JA. Targeting GSK3 and associated signaling pathways involved in cancer. Cells 2020; 9: 1110.

[10] Ougolkov AV, Fernandez-Zapico ME, Savoy DN, Urrutia RA and Billadeau DD. Glycogen synthase kinase-3 beta participates in nuclear factor kappaB-mediated gene transcription and cell survival in pancreatic cancer cells. Cancer Res 2005; 65: 2076-81.

[11] Kunnimalaiyaan S, Gamblin TC and Kunnimalaiyaan M. Glycogen synthase kinase-3 inhibitor AR-A014418 suppresses pancreatic cancer cell growth via inhibition of GSK-3-mediated Notch1 expression. HPB (Oxford) 2015; 17: 770-6.

[12] Mamaghani S, Patel S and Hedley DW. Glycogen synthase kinase-3 inhibition disrupts nuclear factor-kappaB activity in pancreatic cancer, but fails to sensitize to gemcitabine chemotherapy. BMC Cancer 2009; 9: 132.

[13] Shimasaki T, Ishigaki Y, Nakamura Y, Takata T, Nakaya N, Nakajima H, Sato I, Zhao X, Kitano A, Kawakami K, Tanaka T, Takegami T, Tomosugi N, Minamoto T and Motoo Y. Glycogen synthase kinase 3-beta inhibition sensitizes pancreatic cancer cells to gemcitabine. J Gastroenterol 2012; 47: 321-33.

[14] Uehara M, Domoto T, Takenaka S, Bolidong D, Takeuchi O, Miyashita T and Minamoto T. Glycogen synthase kinase-3β participates in acquired resistance to gemcitabine in pancreatic cancer. Cancer Sci 2020; 111: 4405-16.

[15] Ding L, Madamsetty VS, Kiers S, Alekhina O, Ugolkov A, Dube J, Zhang Y, Zhang J, Wang E, Dutta SK, Schmitt DM, Giles FJ, Kozikowski AP, Mazar AP, Mukhopadhyay D and Billadeau DD. Glycogen synthase kinase-3 inhibition sensitizes pancreatic cancer cells to chemotherapy by abrogating the TopBP1/ATR-mediated DNA damage response. Clin Cancer Res 2019; 25: 6452-62.

[16] Hao Q, Gao L, Niu W, Chen L, Zhang P and Chen Z. POTEE stimulates the proliferation of pancreatic cancer by activating the PI3K/Akt/

GSK-3β/β-catenin signaling. Biofactors 2020; 46: 685-92.
[17] Santoro R, Zanotto M, Simionato F, Zecchetto C, Merz V, Cavallini C, Piro G, Sabbadini F, Boschi F, Scarpa A and Melisi D. Modulating TAK1 expression inhibits YAP and TAZ oncogenic functions in pancreatic cancer. Mol Cancer Ther 2020; 19: 247-57.
[18] Vasdev N, Garcia A, Stableford WT, Young AB, Meyer JH, Houle S and Wilson AA. Synthesis and ex vivo evaluation of carbon-11 labelled N-(4-methoxybenzyl)-N'-(5-nitro-1,3-thiazol-2-yl)urea ([^{11}C]AR-A014418): a radiolabelled glycogen synthase kinase-3beta specific inhibitor for PET studies. Bioorg Med Chem Lett 2005; 15: 5270-3.
[19] Cole EL, Shao X, Sherman P, Quesada C, Fawaz MV, Desmond TJ and Scott PJ. Synthesis and evaluation of [^{11}C]PyrATP-1, a novel radiotracer for PET imaging of glycogen synthase kinase-3β (GSK-3β). Nucl Med Biol 2014; 41: 507-12.
[20] Li L, Shao X, Cole EL, Ohnmacht SA, Ferrari V, Hong YT, Williamson DJ, Fryer TD, Quesada CA, Sherman P, Riss PJ, Scott PJ and Aigbirhio FI. Synthesis and initial in vivo studies with [^{11}C] SB-216763: the first radiolabeled brain penetrative inhibitor of GSK-3. ACS Med Chem Lett 2015; 6: 548-52.
[21] Kumata K, Yui J, Xie L, Zhang Y, Nengaki N, Fujinaga M, Yamasaki T, Shimoda Y and Zhang M. Radiosynthesis and preliminary PET evaluation of glycogen synthase kinase 3β (GSK-3β) inhibitors containing [^{11}C]methylsulfanyl, [^{11}C] methylsulfinyl or [^{11}C]methylsulfonyl groups. Bioorg Med Chem Lett 2015; 25: 3230-3.
[22] Hu K, Patnaik D, Collier TL, Lee KN, Gao H, Swoyer MR, Rotstein BH, Krishnan HS, Liang SH, Wang J, Yan Z, Hooker JM, Vasdev N, Haggarty SJ and Ngai M. Development of [^{18}F]maleimide-based glycogen synthase kinase-3β ligands for positron emission tomography imaging. ACS Med Chem Lett 2017; 8: 287-92.
[23] Prabhakaran J, Sai KKS, Sattiraju A, Mintz A, Mann JJ and Kumar JSD. Radiosynthesis and evaluation of [^{11}C]CMP, a high affinity GSK3 ligand. Bioorg Med Chem Lett 2019; 29: 778-81.
[24] Zhong Y, Yang S, Cui J, Wang J, Li L, Chen Y, Chen J, Feng P, Huang S, Li H, Han Y, Tang G and Hu K. Novel ^{18}F-labeled isonicotinamide-based radioligands for positron emission tomography imaging of glycogen synthase kinase-3β. Mol Pharm 2021; 18: 1277-84.
[25] Giglio J, Fernandez S, Martinez A, Zeni M, Reyes L, Rey A and Cerecetto H. Glycogen synthase kinase-3 maleimide inhibitors as potential PET-tracers for imaging Alzheimer's disease: ^{11}C-synthesis and in vivo proof of concept. J Med Chem 2021; [Epub ahead of print].
[26] Varlow C, Mossine AV, Bernard-Gauthier V, Scott PJH and Vasdev N. Radiofluorination of oxazole-carboxamides for preclinical PET neuroimaging of GSK-3. J Fluor Chem 2021; 245: 109760.
[27] Liang SH, Chen JM, Normandin MD, Chang JS, Chang GC, Taylor CK, Trapa P, Plummer MS, Para KS, Conn EL, Lopresti-Morrow L, Lanyon LF, Cook JM, Richter KE, Nolan CE, Schachter JB, Janat F, Che Y, Shanmugasundaram V, Lefker BA, Enerson BE, Livni E, Wang L, Guehl NJ, Patnaik D, Wagner FF, Perlis R, Holson EB, Haggarty SJ, El Fakhri G, Kurumbail RG and Vasdev N. Discovery of a highly selective glycogen synthase kinase-3 inhibitor (PF-04802-367) that modulates tau phosphorylation in the brain: translation for PET neuroimaging. Angew Chem Int Ed Engl 2016; 55: 9601-5.
[28] Bernard-Gauthier V, Mossine AV, Knight A, Patnaik D, Zhao WN, Cheng C, Krishnan HS, Xuan LL, Chindavong PS, Reis SA, Chen JM, Shao X, Stauff J, Arteaga J, Sherman P, Salem N, Bonsall D, Amaral B, Varlow C, Wells L, Martarello L, Patel S, Liang SH, Kurumbail RG, Haggarty SJ, Scott PJH and Vasdev N. Structural basis for achieving GSK-3β inhibition with high potency, selectivity, and brain exposure for positron emission tomography imaging and drug discovery. J Med Chem 2019; 62: 9600-17.
[29] Knight AC, Varlow C, Tong J and Vasdev N. In vitro and in vivo evaluation of GSK-3 radioligands in Alzheimer's disease: preliminary evidence of sex differences. ACS Pharmacol Transl Sci 2021; 4: 1287-94.
[30] Wilson AA, Garcia A, Houle S and Vasdev N. Utility of commercial radiosynthetic modules in captive solvent [^{11}C]-methylation reactions. J Labelled Comp Radiopharm 2009; 52: 490-492.
[31] Mamaghani S, Simpson CD, Cao PM, Cheung M, Chow S, Bandarchi B, Schimmer AD and Hedley DW. Glycogen synthase kinase-3 inhibition sensitizes pancreatic cancer cells to TRAIL-induced apoptosis. PLoS One 2012; 7: e41102.
[32] Boyle AJ, Tong J, Zoghbi SS, Pike VW, Innis RB and Vasdev N. Repurposing [^{11}C]PS13 for PET imaging of cyclooxygenase-1 in ovarian cancer xenograft mouse models. J Nucl Med 2021; 62: 665-668.
[33] Moran MD, Wilson AA, Elmore CS, Parkes J, Ng A, Sadovski O, Graff A, Daskalakis ZJ, Houle S, Chapdelaine MJ and Vasdev N. Development of new carbon-11 labelled radiotracers for imaging $GABA_A$- and $GABA_B$-benzodiazepine receptors. Bioorg Med Chem 2012; 20: 4482-8.
[34] Lin SF, Bois F, Holden D, Nabulsi N, Pracitto R, Gao H, Kapinos M, Teng J, Shirali A, Ropchan J, Carson RE, Elmore CS, Vasdev N and Huang Y. The search for a subtype-selective PET imag-

ing agent for the $GABA_A$ receptor complex: evaluation of the radiotracer [^{11}C]ADO in nonhuman primates. Mol Imaging 2017; 16: 1536012117731258.

[35] Wilson W 3rd and Baldwin AS. Maintenance of constitutive IkappaB kinase activity by glycogen synthase kinase-3alpha/beta in pancreatic cancer. Cancer Res 2008; 68: 8156-63.

[36] Edderkaoui M, Chheda C, Soufi B, Zayou F, Hu RW, Ramanujan VK, Pan X, Boros LG, Tajbakhsh J, Madhav A, Bhowmick NA, Wang Q, Lewis M, Tuli R, Habtezion A, Murali R and Pandol SJ. An inhibitor of GSK-3β and HDACs kills pancreatic cancer cells and slows pancreatic tumor growth and metastasis in mice. Gastroenterology 2018; 155: 1985-98, e5.

[37] Ougolkov AV, Fernandez-Zapico ME, Bilim VN, Smyrk TC, Chari ST and Billadeau DD. Aberrant nuclear accumulation of glycogen synthase kinase-3beta in human pancreatic cancer: association with kinase activity and tumor dedifferentiation. Clin Cancer Res 2006; 12: 5074-81.

[38] Pecoraro C, Faggion B, Balboni B, Carbone D, Peters GJ, Diana P, Assaraf YG and Giovannetti E. GSK-3β as a novel promising target to overcome chemoresistance in pancreatic cancer. Drug Resist Updat 2021; 58: 100779.

[39] Watson RL, Spalding AC, Zielske SP, Morgan M, Kim AC, Bommer GT, Eldar-Finkelman H, Giordano T, Fearon ER, Hammer GD, Lawrence TS and Ben-Josef E. GSK-3beta and beta-catenin modulate radiation cytotoxicity in pancreatic cancer. Neoplasia 2010; 12: 357-65.